ADVANCED FUNCTIONAL MATERIALS
www.afm-journal.de

Synergistic Compositional–Mechanical–Thermal Effects Leading to a Record High zT in n-Type V_2VI_3 Alloys Through Progressive Hot Deformation

Lipeng Hu, Yang Zhang, Haijun Wu, Yamei Liu, Junqin Li, Jian He, Weiqin Ao, Fusheng Liu, Stephen John Pennycook, and Xierong Zeng*

Here a progressive hot deformation procedure that endows the benchmark n-type V_2VI_3 thermoelectric materials with short range disorder (multiple defects), long range order (crystallinity), and strong texture (nearly orientation order) is reported. Not only it is rare for these structural features to coexist but also these structural features elicit the synergistic compositional–mechanical–thermal effects, i.e., a profound interplay among the counts, magnitude, and temperature of hot deformation in relation to the as formed point defects, dislocations, textures, strain clusters, and distortions. Using progressively larger die sets and relatively low hot deformation temperature, rich multiscale microstructures concurrently with a high level of texture comparable to that of zone melted ingot are obtained. The strong donor-like effect significantly increases the majority carrier concentration, suppressing the detrimental bipolar effect. In addition, the multiscale microstructures yield an ultralow lattice thermal conductivity ≈0.31 W m^{-1} K^{-1} at 405 K. A record zT ≈ 1.3 at 450 K are attained in progressively hot deformed n-type $Bi_{1.95}Sb_{0.05}Te_{2.3}Se_{0.7}$ through the synergistic effects. These results not only promise a better pairing between n-type and p-type legs in device fabrication but also bring our understanding of n-type V_2VI_3 alloys and hot deformation technique to a new level.

1. Introduction

With the capability of direct heat-electricity energy conversion without greenhouse emissions, thermoelectrics provides a solution to the global energy and environmental crisis.[1] The efficiency of a thermoelectric (TE) device is governed by the device material's figure of merit, $zT = \sigma S^2 T/\kappa$, where T, σ, S, and κ are the absolute temperature, the electrical conductivity, the Seebeck coefficient, and the total thermal conductivity (including the lattice component κ_{ph} and the charge carrier component κ_{el}), respectively. Toward higher zT, defect engineering is invoked to (i) improve the power factor PF = σS^2 through tuning band structure,[2,3] texture,[4,5] and grain boundary;[6,7] and (ii) suppress the κ_{ph} through multiscale microstructures.[8,9] While point defects are of vital importance,[10,11] it is the synergy among various kinds of defects in defect engineering that underlies the high zT.

The rhombohedral V_2VI_3 materials are a hotbed of defect engineering,[12] the success of which make them the benchmark TE materials for solid-state cooling[8,13,14] and low/mid temperature waste heat harvesting.[15–24] In particular, the high performance of n-type V_2VI_3 alloys is subject to a delicate balance between strong textures and multiscale microstructures, which is a challenge for materials synthesis and processing. Making the task more challenging, the performance-enhancing mechanisms proved effective in p-type V_2VI_3 alloys turned out to be less so in n-type V_2VI_3 alloys. Compared to the p-type counterpart, the n-type V_2VI_3 material tends to be electrically more anisotropic: the electrical conductivity anisotropy of

Dr. L. P. Hu, Prof. J. Q. Li, Prof. W. Q. Ao, Prof. F. S. Liu, Prof. X. R. Zeng
College of Materials Science and Engineering
Shenzhen University, and Shenzhen Key Laboratory
of Special Functional Materials
Shenzhen 518060, P. R. China
E-mail: junqinli@szu.edu.cn

Dr. L. P. Hu, Prof. X. R. Zeng
Key Laboratory of Optoelectronic Devices and Systems
of Ministry of Education and Guangdong Province
College of Optoelectronic Engineering
Shenzhen University
Shenzhen 518060, P. R. China

Y. Zhang, H. J. Wu, Prof. S. J. Pennycook
Department of Materials Science and Engineering
National University of Singapore
7 Engineering Drive 1, Singapore 117575, Singapore

Y. M. Liu, Prof. J. He
Department of Physics and Astronomy
Clemson University
Clemson, SC 29634-0978, USA

The ORCID identification number(s) for the author(s) of this article can be found under https://doi.org/10.1002/adfm.201803617.

DOI: 10.1002/adfm.201803617

n-type V_2VI_3 single crystal (≈ 4–7) is higher than that of the p-type counterpart (≈3).[25] A high level of (00*l*) texture in n-type V_2VI_3 alloys is indispensable for a high charge carrier mobility μ_H and a large PF (≈4 W m^{-1} K^{-2}).[8,13] For example, n-type V_2VI_3 alloys prepared by hot pressing (HP) or spark plasma sintering (SPS) are not highly (00*l*)-textured, their maximum zT values are no higher than 1.0.[8,13,14] Due to a nanoscale carrier mean free path in n-type V_2VI_3 alloys,[8] the grain refinement or nanostucturing approach, which effectively suppresses the κ_{ph}, severely degrades the μ_H and the PF.

There are several other peculiarities about n-type V_2VI_3 alloys. First, the optimal composition varies drastically with the micromorphology. The optimal composition for mechanically deformed polycrystalline n-type $Bi_2Te_{3-x}Se_x$ (typically via grinding or ball milling) is $Bi_2Te_{2.3}Se_{0.7}$ while the counterpart for single crystals (SC) or zone melted (ZM) ingots is $Bi_2Te_{2.7}Se_{0.3}$.[10] Second, the carrier concentration n_H, the key transport parameter for high zT, is directly governed by the intrinsic point defects (mainly antisites and anion vacancies) that can be further regulated chemically, mechanically, and thermally.[10] This causal chain is crucial in that tuning the intrinsic point defects affords a way to optimize the n_H without invoking the use of unstable (Ag and Cu) and expensive donors (SbI_3 or TeI_4) dopants.[8,10] Third, the texture of V_2VI_3 alloys relies on crystal slip along the basal plane with the aid of dislocation movement under pressure, which is accompanied by the generation and annihilation of intrinsic point defects.[26] High density dislocations can effectively scatter the mid-wavelength phonons that are less effectively affected by point defects and grain boundaries.[8,17]

Hence, implementing desired microstructures, optimizing intrinsic point defects while retaining a high level of (00*l*) texture pose a challenge in material synthesis and processing of n-type V_2VI_3 alloys. To this end, hot deformation (HD) is a promising approach.[10] HD has been implemented in p- and n-type V_2VI_3 solid solutions, which enhanced the (00*l*) textures to some extent, induced atomic scale point/line defects and nanoscale distortions, and also tuned the n_H through the donor-like effect.[8,10,18,20,27] Despite the progress, there are at least three specific barriers impeding HD from further improving the zT of n-type V_2VI_3 alloys. The first barrier is that the texture nearly remains unchanged when the number of times of HD process is more than twice using the same small die set.[4,28] Second, in view of the small band gap of V_2VI_3 alloys and the purpose of waste heat harvesting at elevated temperature, the donor-like effect needs to be strong enough to afford a higher majority carrier concentration to suppress the detrimental bipolar effect.[20,29] Previous studies showed that at a low degree of deformation, the donor-like effect is quickly saturated with increasing number of HD (aka the HD count); deformation at high temperature induces the recovery effect that weakens the donor-like effect,[4] high HD temperatures (773 or 823 K) also lead to grain coarsening that is less favored for suppressing the κ_{ph}.[4,8] Furthermore, high energy ball milling yields a strong donor like effect, but the high degree of texture is irreversibly lost.

We herein adopt a strategy based on the hot deformation induced "synergistic compositional–mechanical–thermal effects" in n-type polycrystalline V_2VI_3 alloys. This strategy aims at the peculiarities of n-type V_2VI_3 alloys and those specific barriers of traditional HD process. The additive-based (chemical), deformation-based (mechanical), and thermal-based (thermal) effects and the resulting interplay among the intrinsic and extrinsic point defects, textures, dislocations, nanoscale strain clusters and distortions constitute the core of synergistic compositional–mechanical–thermal effects. These synergistic effects are implemented through an innovative HD procedure with progressively greater degree of deformation, higher HD counts, but lower HD temperature. We found that the optimal HD temperature 723 K is the balance point between the donor-like effect and the recovery effect.[30] The innovative hot deformation process endows V_2VI_3 alloys with short range disorder (rich multiscale microstructures), long range order (good crystallinity), and strong texture (preferred orientation), which tend to be counter related in a material. The derived strong (00*l*) texture, comparable to that of ZM ingots, ensures a large PF. The purpose of Sb alloying in the present work is twofold: (i) enhancing mass fluctuation scattering of phonons; and (ii) facilitating the formation of antisite defects and thus enhances the donor-like effect at a relatively low HD temperature. The derived κ_{ph} (≈0.31 W m^{-1} K^{-1} at 405 K) is one of the lowest values reported in V_2VI_3 alloys due to the multiscale microstructures. The resulting record $zT \approx 1.3$ at 450 K and high average zT values of 1.2 between 300 and 500 K for five-time hot deformed $Bi_{1.95}Sb_{0.05}Te_{2.3}Se_{0.7}$ promise a better leg pairing with the p-type V_2VI_3 compounds that have zT values in the range of 1.3–1.8[15–18] in device fabrications.

2. Results and Discussion

The results and discussion are organized as follows. Subsection 2.1 covers the detailed texture evolution as a function of HD conditions. The main theme of Subsection 2.2 is the HD induced multiscale microstructures. Subsection 2.3 addresses the chemistry of intrinisc point defects. In Subsection 2.4, we present the state-of-the-art TE properties in relation to the synergistic compositional–mechanical–thermal effects.

2.1. Evolution of Texture with Hot Deformation

In light of the quaternary Bi–Sb–Se–Te phase diagram (**Figure 1**a) and as shown in Figure 1b,[13,31] single-phased $Bi_{2-x}Sb_xTe_{2.3}Se_{0.7}$ ($0 \le x \le 0.25$) samples with HD count = 1 were obtained, they all adopted a hexagonal crystal structure (JCPDS# 29-0247). All peaks shift toward higher angles with increasing Sb content, indicating the formation of solid solutions. The basal lattice parameter is nearly unchanged, while the axial lattice parameter drops gradually with increasing Sb content, consistent with the smaller radius of Sb atom (1.45 Å) compared to that of Bi atom (1.60 Å) (Figure S1, Supporting Information). The progressive hot deformed $Bi_{1.95}Sb_{0.05}Te_{2.3}Se_{0.7}$ samples still retain a hexagonal structure without discernible secondary phases (Figure 1c).

As mentioned above, retaining a high level of texture is vital for the high zT of n-type polycrystalline V_2VI_3 alloys. The degree of texture and the textural evolution with Sb content and

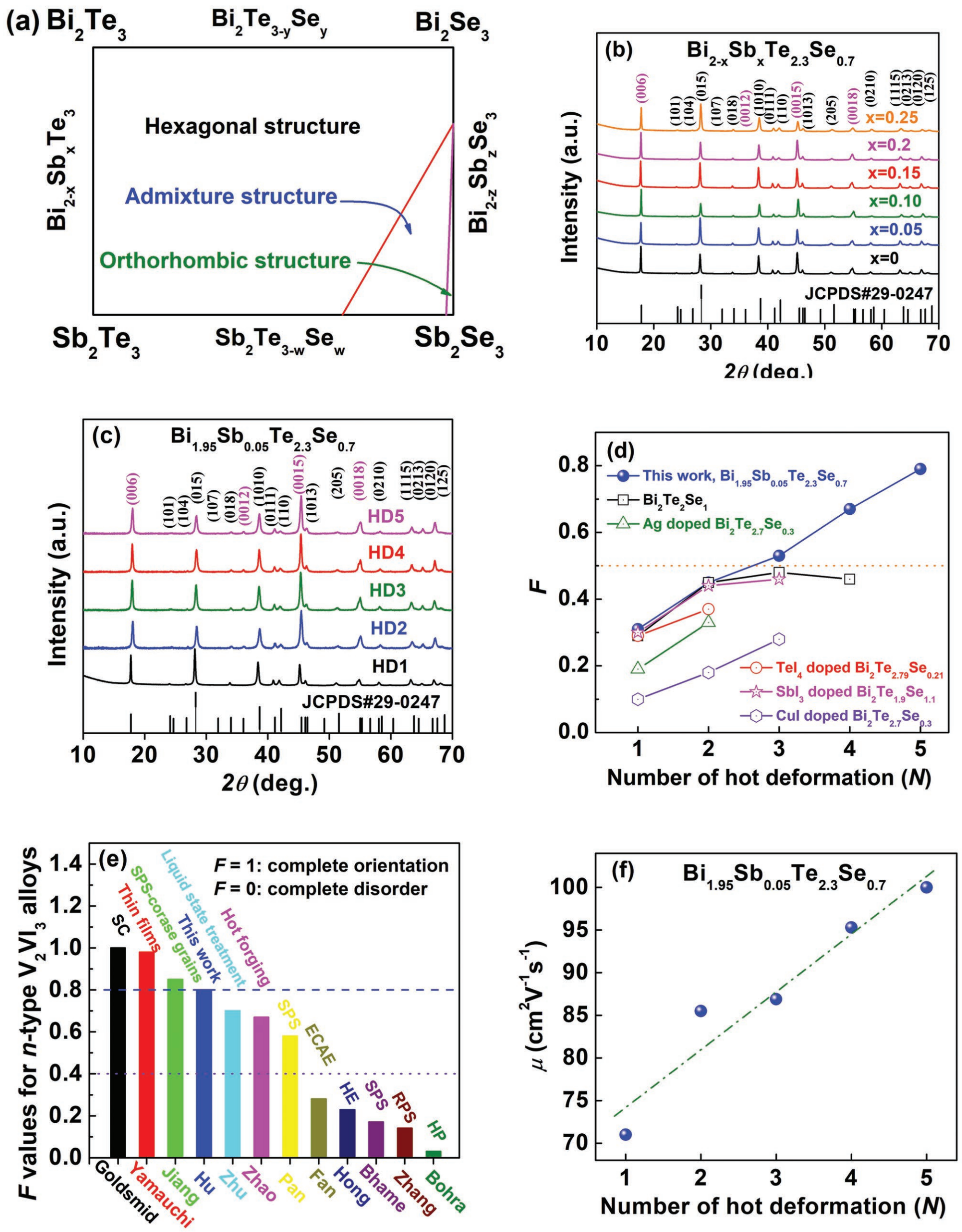

Figure 1. a) Phase diagram of Bi_2Te_3-Bi_2Se_3-Sb_2Te_3-Sb_2Se_3 system, obtained in ref. [31] XRD patterns for b) $Bi_{2-x}Sb_xTe_{2.3}Se_{0.7}$ (x = 0–0.25) samples with HD count = 1, and c) $Bi_{1.95}Sb_{0.05}Te_{2.3}Se_{0.7}$ samples with different HD count. d) F values[4,8,28,32,33] and f) carrier mobility as a function of HD count. e) F values in this work in comparison with those of other n-type V_2VI_3 alloys.[25,27,34–42]

HD count can be gauged by the orientation degree F of (00l) planes (Figure S2, Supporting Information and Figure 1d).[43] Ideally, $F = 1$ for single crystal and $F = 0$ for complete random orientation. The F value is nearly unchanged with varying Sb content, while rapidly rises with increasing HD count. It is known that the grains easily slip and rotate along the basal planes under pressure and the c-axis tends to be aligned parallel to the pressing direction during the plastic deformation process, thereby leading to a substantially enhanced (00l) textures. Though such phenomena were observed in early works of $Bi_2Te_{3-x}Se_x$ alloys,[4,8,32,33] the degree of texture obtained therein is generally weaker than that is derived in this work. The cause of this discrepancy allows us to have a deeper understanding of the HD process and also the n-type V_2VI_3 alloys.

The HD count, degree and temperature are three pivotal parameters to obtain strong (00l) texture. **Table 1** summarizes the major HD parameters and the derived F values in the present and some prior works.[4,8,32] There are some interesting findings. First of all, deformation in a larger graphite die is generally beneficial for texture enhancement. In this work, a progressively larger magnitude of deformation (in progressively larger die sets) led to consistently enhanced texture with increasing HD count. Second, comparing the present work with ref. [28], the derived (00l) texture or the F value is not solely

Table 1. Majority deformation parameters and *F* values in this and prior work.

	This work			Ref. [4]			Ref. [28]			Ref. [32]		
	ε	T [K]	F	ε	T [K]	F	ε	T [K]	F	ε	T [K]	F
HD1	10–12.7	773	0.31	10–12.7	823	0.29	10–16	823	0.30	10–11	603	0.10
HD2	12.7–15	723	0.45	10–12.7	823	0.45	16–20	823	0.44	11–12.7	603	0.18
HD3	15–20	723	0.53	12.7–16	823	0.48	20–25	823	0.46	12.7–15	603	0.28
HD4	20–25	723	0.67	12.7–16	823	0.45	–	–	–	–	–	–
HD5	25–30	723	0.79	–	–	–	–	–	–	–	–	–

determined by the initial and final die size but also subject to the details of intermediate deformations. Third, plastic deformation and dynamic recrystallization (aka the recovery effect) are two counter effects in the HD process, the HD temperature is the key control parameter to attain the balance. A low HD temperature (e.g., 603 K in ref. [32]) failed to reach a uniform plastic deformation and a high degree of texture. On the other hand, a high HD temperature (e.g., 823 K in refs. [4] and [28]) facilitated uniform plastic deformation and thereby significantly enhanced the (00*l*) texture. However, such a high HD temperature also promoted dynamic recrystallization that weakened the texture to some extent because of the reconstruction and rearrangement of grain boundaries.[4,28] In this work, we found an optimized the HD temperature at 723 K, which balanced the plastic deformation and dynamic recrystallization. As a result, the derived *F* value is higher than those of n-type V_2VI_3 polycrystalline alloys,[27,36–42] and is close to that of Bi_2Te_3 thin film[34] and single crystal[25] (Figure 1e).

In order to obtain the complete information of texture and the distribution of crystallographic orientations, the measured and calculated (006), (015), (1010), and (0015) pole figures (abbreviated as MPF and CPF) of the HD1, HD3, and HD5 samples are presented in **Figure 2** and Figures S3–S5 (Supporting Information), respectively. It is concluded that the hot deformed V_2VI_3 materials possess a typical planar texture because all the samples exhibit highest pole density in the middle of (006) pole figures. A higher level of the scale bar indicates a stronger texture. With increasing HD count and degree of deformation, the enhanced degree of texture as reflected in the (006) pole indicates a preferred orientation along (00*l*). More interestingly, the CPF analysis of representative samples reveals the (006) deflect a certain angle along the rolling direction, yielding a bimodal texture for HD1 sample. The deflection angle gradually diminished when the HD count increases to three times. Further increasing the HD count, the (006) is nearly perpendicular to the pressure direction. These results of pole figures clearly show that the grain rearrangement along the (00*l*) due to the severe plastic deformation with larger deformation degree, more deformation count and an appropriate temperature.[4,8]

The orientation distribution function (ODF) was also calculated based on the pole figures and presented in **Figure 3** and Figures S6–S8 (Supporting Information). It is found that two textures, the (00*l*) ⟨10-10⟩ texture located in (000) (6000), while the (00*l*) ⟨2-1-10⟩ texture laid in the (3000) (6000), both belong to (00*l*) planar texture. Apparently, the hot deformation forced the basal plane to orient preferentially perpendicular to the pressure direction. Consistent with the results of previous pole figure analysis, the texture is consistently enhanced by progressive HD via grain rotation and preferential grain growth. In particular, HD5 sample owns especially strong (00*l*) planar texture, which is comparable to that of ZM ingots.[8]

2.2. Multiscale Microstructures

Strong (00l) texture facilitates charge transport but the same also boosts phonon transport that is undesired for high zT values. In order to suppress the κ_{ph} while retaining the μ_H, forming multiscale microstructures with a strong degree of texture via HD is perceived as a feasible way. To showcase the as formed microstructures, the HD5 sample was subject to more detailed microstructural analysis using transmission electron microscopy (TEM). **Figure 4** shows three types of nanoscale structures: strain clusters, polycrystals, and distortions. Figure 4a,b is the low- and mediate-magnification TEM images of the HD5 sample, plastic deformation induced a high density of nanoscale strain clusters are observed. As shown in Figure 4c, nanocrystals with the size of ≈60 nm embedded in the matrix can be readily observed through the sample, similar to previous report.[8] These embedded nanocrystals come from the dynamic recrystallization during the hot deformation process. Meanwhile, the highly deformed sample displays a mass of nanoscale distorted regions, because amounts of slips form to comply with strain compatibility during severe deformation (Figure 4d).

The other characteristic structural feature is the high density of dislocations as shown in Figure 4e. A larger degree of HD at a lower temperature would induce more severe plastic deformation, which creates a large number of dislocations inside the distorted regions as well as at the interfaces between the distorted regions and the matrix. Dislocation scattering has been proved to be effective in scattering midwavelength phonons,[17] thus dense dislocations induced by innovative HD promise a significant reduction of κ_{ph}. Furthermore, hot deformation also produces atomic-scale intrinsic point defects (i.e., vacancies) into the lattice that further impede the transport of short-wavelength phonons. As such, the progressive HD creates multiscale structural defects, including microscale grain boundaries, nanoscale strain clusters, polycrystals, and distortions, as well as atomic-scale point and line defects, which work synergistically to realize full-spectrum phonon scatterings, thereby substantially suppressing the κ_{ph} over a wide temperature range.

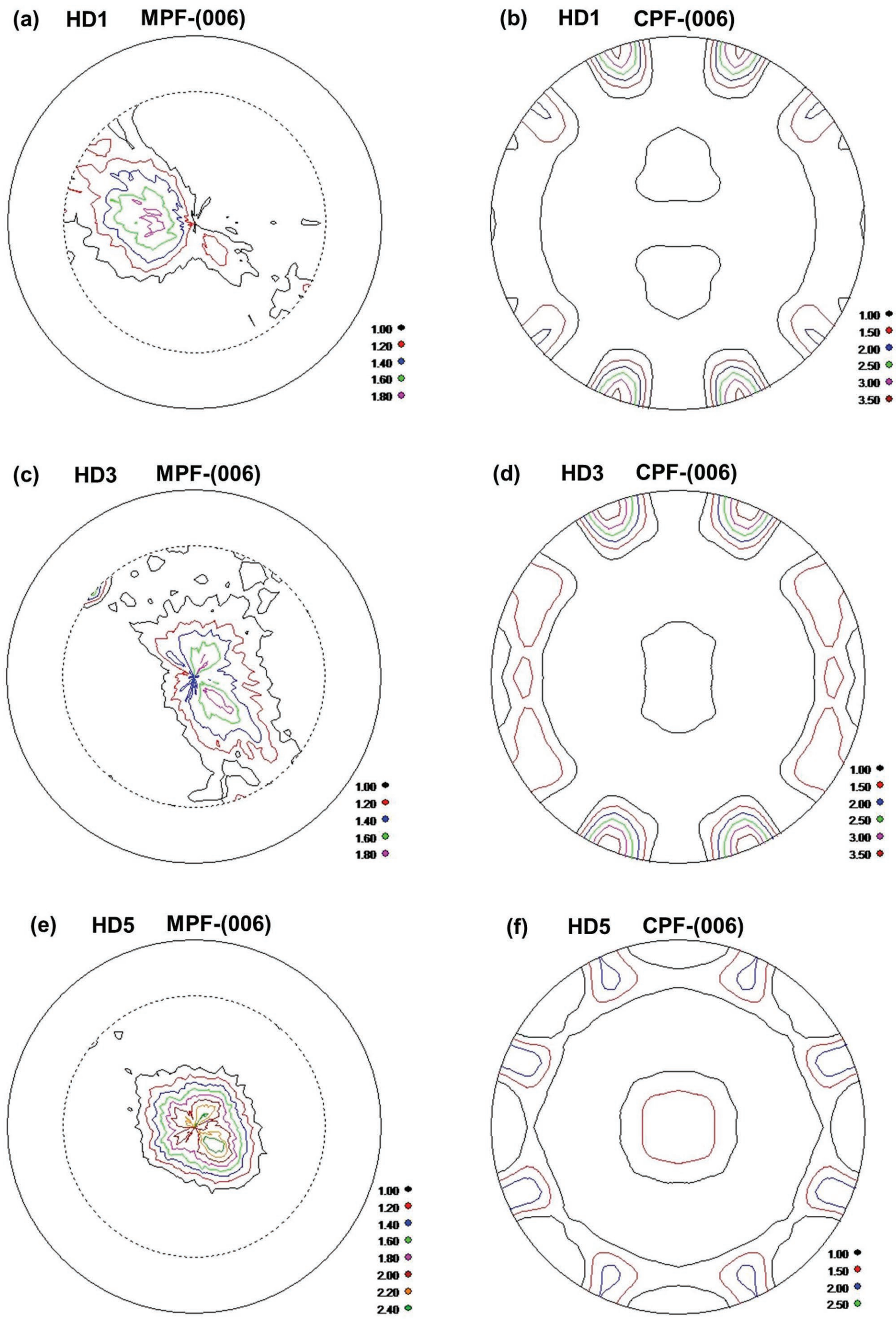

Figure 2. The (006) MPF and CPF of the $Bi_{1.95}Sb_{0.05}Te_{2.3}Se_{0.7}$ polycrystalline samples with different hot deformation number: a) HD1, b) HD3, and c) HD5 (taken on the polished surfaces for all the samples).

2.3. Carrier Concentration in Relation to Intrinsic Point Defects

The μ_H of $Bi_{1.95}Sb_{0.05}Te_{2.3}Se_{0.7}$ is remarkably increased upon enhanced (00*l*) texture despite the formation of multiscale microstructures after progressive HD process (Figure 1f). The room temperature μ_H substantially increases from 71 $cm^2\ V^{-1}\ S^{-1}$ at $n_H = 6.9 \times 10^{19}\ cm^{-3}$ for the HD1 sample to 100 $cm^2\ V^{-1}\ S^{-1}$ at $n_H = 9.7 \times 10^{19}\ cm^{-3}$ for the HD5 sample. For comparison, the μ_H of SC $Bi_2Te_{2.4}Se_{0.6}$ is 149 $cm^2\ V^{-1}\ S^{-1}$ at a $n_H = 4.1 \times 10^{19}\ cm^{-3}$.[44]

With a strong textures and multiscale microstructures, we shift our focus to the optimization of n_H, another key electrical transport parameter. Previous works demonstrated that the n_H of V_2VI_3 compounds is directly governed by the type and

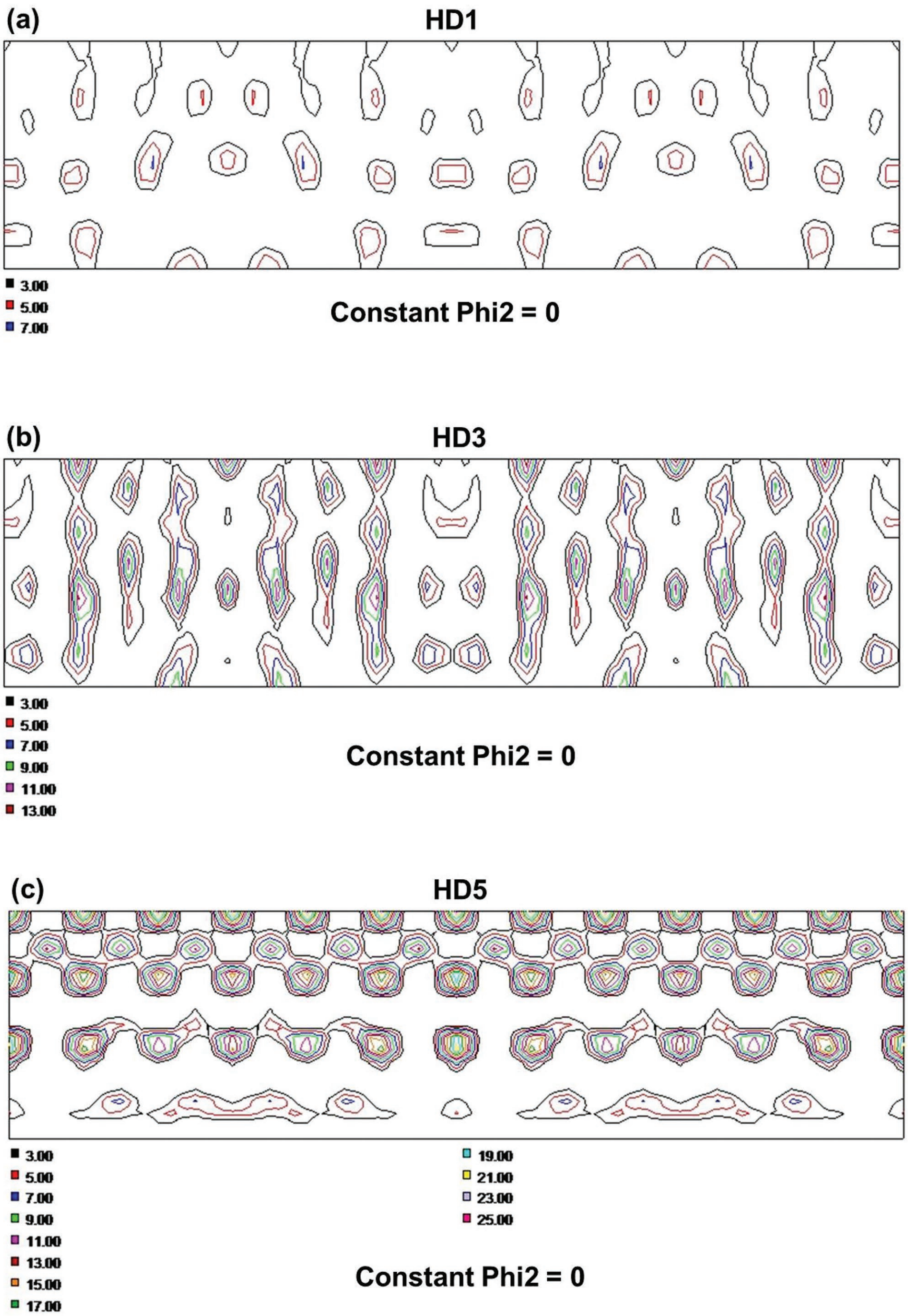

Figure 3. ODF patterns of the $Bi_{1.95}Sb_{0.05}Te_{2.3}Se_{0.7}$ polycrystalline samples with different hot deformation number: a) HD1, b) HD3, and c) HD5 (taken on the polished surfaces for all the bulk samples).

amount of intrinsic point defect (**Figure 5**a).[10,12] As shown Figure 5b, the n_H of n-type polycrystalline $Bi_{2-x}Sb_xTe_{2.3}Se_{0.7}$ initially rises and then drops with increasing Sb content (i.e., the x value), pointing toward the interplay between the extrinsic and intrinsic point defects. There are two major sources of intrinsic point defects in deformed $Bi_{2-x}Sb_xTe_{2.3}Se_{0.7}$. The first source is of chemical origin: the antisite defects (Bi'_{Te} or Bi'_{Se}) are formed during the growth of $Bi_2Te_{3-x}Se_x$ from the melts.[10] Reducing the difference in electronegativity $\Delta\chi$ between the cation and the anion facilitates the formation of antisite defects.[10] Hence, the addition of Sb into $Bi_2Te_{3-x}Se_x$ increases the concentration of antisites $[Bi'_{Te}]$ on account of the smaller $\Delta\chi$ of Sb–Te ($\Delta\chi = 0.05$) than that of Bi–Te ($\Delta\chi = 0.08$). The other source is of mechanical origin: the deformation induced nonbasal slips yield, on the average, pairs of $2V'''_{Bi}$ and $3V^{\bullet\bullet}_{Te}$. In the presence of abundant Bi vacancies, the antisites Bi'_{Te} readily diffuse back

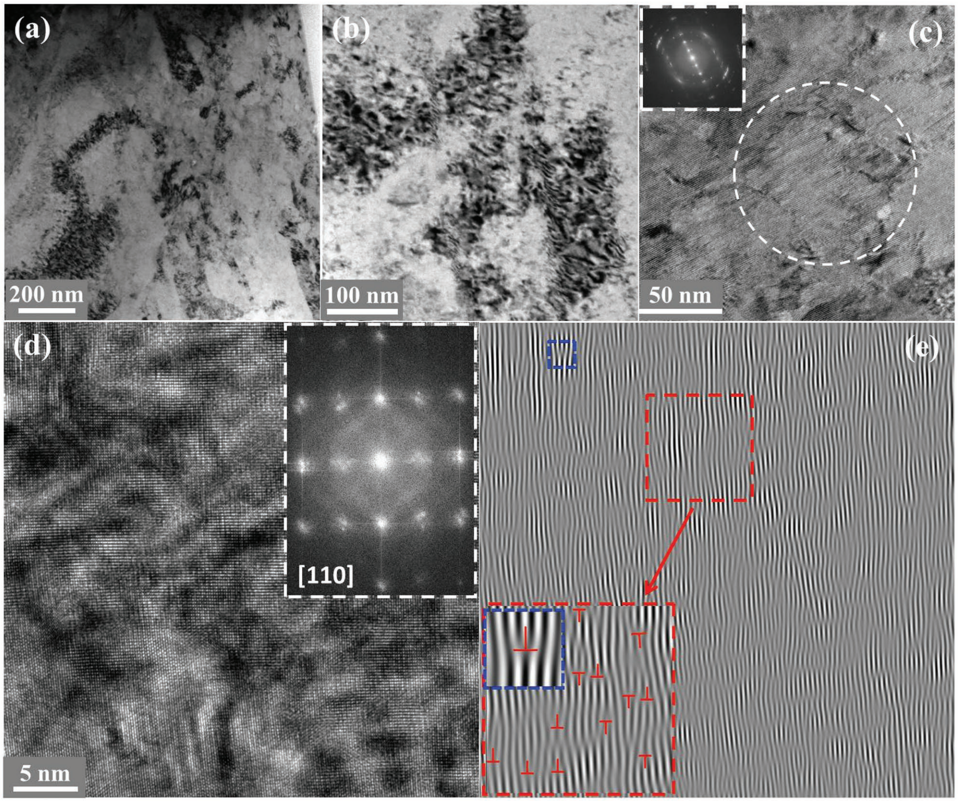

Figure 4. Structures of the HD5 sample: a) low- and b) mediate-magnification TEM images showing high strain clusters. c) HRTEM image showing nanoscale polycrystals. d) HRTEM image showing lattices with severe distortions, with its fast Fourier transform (FFT) image inset. e) Inverse FFT image showing a high density of dislocations, with an enlarged image in inset.

into the Bi sublattice, creating excess anion vacancies $V_{Te}^{\bullet\bullet}$ (i.e., the donor-like defects) and electrons. This is referred as the donor-like effect[10]

$$2V_{Bi}''' + 3V_{Te}^{\bullet\bullet} + Bi_{Te}' \rightarrow V_{Bi}''' + Bi_{Bi}^{x} + 4V_{Te}^{\bullet\bullet} + 6e' \quad (1)$$

The same formula is valid for V_{Sb}''', $V_{Se}^{\bullet\bullet}$, Sb_{Te}', Sb_{Se}', and Bi_{Se}'.

Equation (1) correlates the chemically created antisites Bi_{Te}' and mechanically created donor-like defects $V_{Te}^{\bullet\bullet}$, alowing us to interpret the results presented in Figure 5a. For the ease of discussion, it is plausible to assume that all $Bi_{2-x}Sb_xTe_{2.3}Se_{0.7}$ samples have the same $[V_{Bi}''']$ and $[V_{Te}^{\bullet\bullet}]$ as they were subject to the same grain refinement and HD process. At $x = 0$, the $[Bi_{Te}']$ is relatively low, the donor-like effect is thus weak in view of Equation (1), giving rise to a low n_H.[45] The initial Sb alloying ($0 < x < 0.10$) increases the $[Bi_{Te}']$ and thus promotes the donor-like effect, yielding an increased n_H (Figure 5a). At a higher Sb content ($x \geq 0.15$), however, a higher $[Bi_{Te}']$ is attained but only part of it contributes to the donor-like effect, the reminder of Bi'_{Te} compensates $V_{Te}^{\bullet\bullet}$, yielding a drastic reduction in n_H. Similar phenomena can be found in polycrystalline $Bi_2Te_{3-x}Se_x$[10] and $Bi_2Te_{2.3}Se_{0.7-x}$[45] systems.

As depicted in Figure S9 of the Supporting Information, a small amount of Sb alloying increases the concentration of antisite defects and promotes the donor-like effect, thereby enhancing the σ and PF. At the same time, the initial incorporation of Sb enhances the scattering of phonons via the lattice distortion and mass fluctuation, which leads to the slight reduction in the κ_{ph}. The double effects of simple Sb alloying yield a highest zT of 1.1 at 405 K for once hot deformed $Bi_{1.95}Sb_{0.05}Te_{2.3}Se_{0.7}$, which is much higher than the HP $Bi_2Te_{2.3}Se_{0.7}$, and comparable to the HD3 $Bi_2Te_{2.3}Se_{0.7}$, especially at low temperatures.[10] This zT-enhancement is ascribed to the simultaneously increased n_H and reduced κ_{ph} through Sb alloying.

As known, the optimal carrier concentration (n_{opt}) depends on temperature as $n_{opt} \propto T^{3/2}$. Previous reports suggested that the n_{opt} near room temperature is about 5×10^{19} cm^{-3} in V_2VI_3 solid solutions.[8,14] For the application of low-temperature power generation at 450 K, the n_{opt} should be raised above 9.2×10^{19} cm^{-3}. Notably, the n_H of $x = 0.05$ HD1 sample is only 6.9×10^{19} cm^{-3}, not high enough for TE application above 450 K. These samples need to be subject to further deformation.

In the following, we focus on the further optimization of n_H for the $x = 0.05$ HD1 sample, which possesses the highest zT value through progressive HD process. As shown in Table S1 of the Supporting Information, the results of energy-dispersive X-ray spectroscopy (EDS) measurements show that the compositions of all the $x = 0.05$ samples slightly deviated from their nominal counterparts due to the Se loss in the growth-from-the-melt process; importantly, the composition is practically unchanged through the progressive HD process. Hence, the observed variation of n_H with the progressive HD process (Figure 5c) is mainly ascribed to the donor-like effect rather than the change of chemical composition.

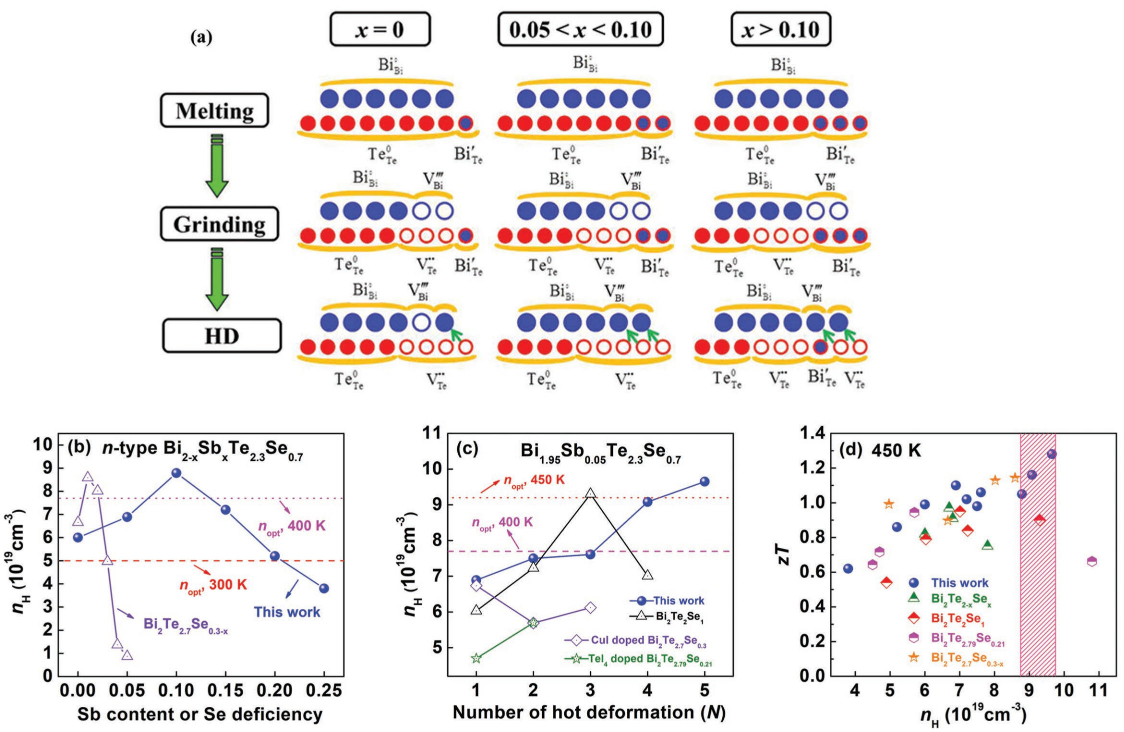

Figure 5. a) Schematic diagram of the variation of intrinsic point defects for $Bi_{2-x}Sb_xTe_{2.3}Se_{0.7}$ materials. Room-temperature carrier concentration of b) n-type $Bi_{2-x}Sb_xTe_{2.3}Se_{0.7}$ polycrystalline alloys as a function of Sb content,[45] and c) n-type $Bi_{1.95}Sb_{0.05}Te_{2.3}Se_{0.7}$ polycrystalline alloys as a function of HD count.[4,8,32] d) zT values at 450 K as a function of carrier concentration in n-type V_2VI_3 system in this and prior work.[4,8,10,45]

In view of Equation (1), more severe deformation produces higher $[V_{Bi}''']$ and $[V_{Te}^{\bullet\bullet}]$ and thus leads to stronger donor-like effect. In this work, our approach is using progressively larger degree of deformation and more deformation times than previous reports (Table 1).[4,8,32] Furthermore, note that the donor-like effect can be mediated by the HD temperature. Below 723 K, the higher the HD temperature the stronger the donor-like effect is. Above 773 K, the recovery effect will offset the donor-like defects to some extent.[30] Variable temperature program (773 K for first time HD and 723 K for the following HDs) is implemented into this work to ensure consistently enhanced donor-like effect. For comparison, the detrimental effect of unoptimized HD temperature on the TE performance is presented in Figure S10 of the Supporting Information.

As depicted in Figure 5c, the room temperature n_H rapidly rises with increasing HD count, substantially higher than those of prior works.[4,8,32] Specially, the HD5 sample owns a room-temperature $n_H \approx 9.7 \times 10^{19}$ cm^{-3}, around 41% increment over the HD1 one. In Figure 5d, we plot the zT values at 450 K versus n_H. It is apparent that the sample with $n_H = 9.7 \times 10^{19}$ cm^{-3} possesses the highest zT around 450 K, which is significantly improved compared with other works.[4,8,10,45]

2.4. The Synergistic Compositional–Mechanical–Thermal Effects and a Record *zT*

With optimized texture (Section 2.1), multiscale microstructures (Section 2.2), and n_H (Section 2.3), we discuss the electrical transport properties of progressively hot deformed $x = 0.05$ sample. As displayed in **Figure 6**a, the σ decreases with temperature for all the samples, typical of degenerate semiconductor behavior. Progressively hot deforming the $x = 0.05$ sample increases the σ because of the simultaneously enhanced textures and donor-like effect. Typically, the room temperature σ of 154×10^3 Sm^{-1} was attained for the HD5 sample, which is a 66% increase than the HD1 one. In addition, the σ for all the samples exhibits a $T^{-3/2}$ dependence, indicative of dominant acoustic phonon scattering.

The influence of HD count on the S is illustrated in Figure 6b. As shown, the room temperature S reduces from −182 μV K^{-1} for the HD1 sample to −169 μV K^{-1} for the HD3 sample, and −155 μV K^{-1} for the HD5 sample, as expected from the increasing n_H.[8] We also note that the peak S shifts from 450 K for the HD1 sample to 480 K for the HD3 sample, and then to 525 K for HD5 one, demonstrating that the adverse impact of intrinsic conduction on the S at the elevated temperature is effectively suppressed. Interestingly, all the HD samples show a similar S value above 550 K. The band gap E_g of $Bi_{2-x}Sb_xTe_{2.3}Se_{0.7}$ was estimated by the Goldsmid–Sharp relationship: $E_g = 2eS_{max}T_{max}$, where the S_{max} peaks at a temperature T_{max}.[20] It is noteworthy that the derived E_g value of $Bi_{2-x}Sb_xTe_{2.3}Se_{0.7}$ alloys is nearly unchanged upon Sb alloying and progressive HD (Tables S2 and S3, Supporting Information). Thus, the suppression of the bipolar effect with increasing HD count is ascribed to the significantly increased majority carriers induced by the donor-like effect. To our best knowledge, this is the first time suppression of intrinsic conduction by donor-like effect without relying on a broadened E_g, is reported in V_2VI_3 solid solutions.

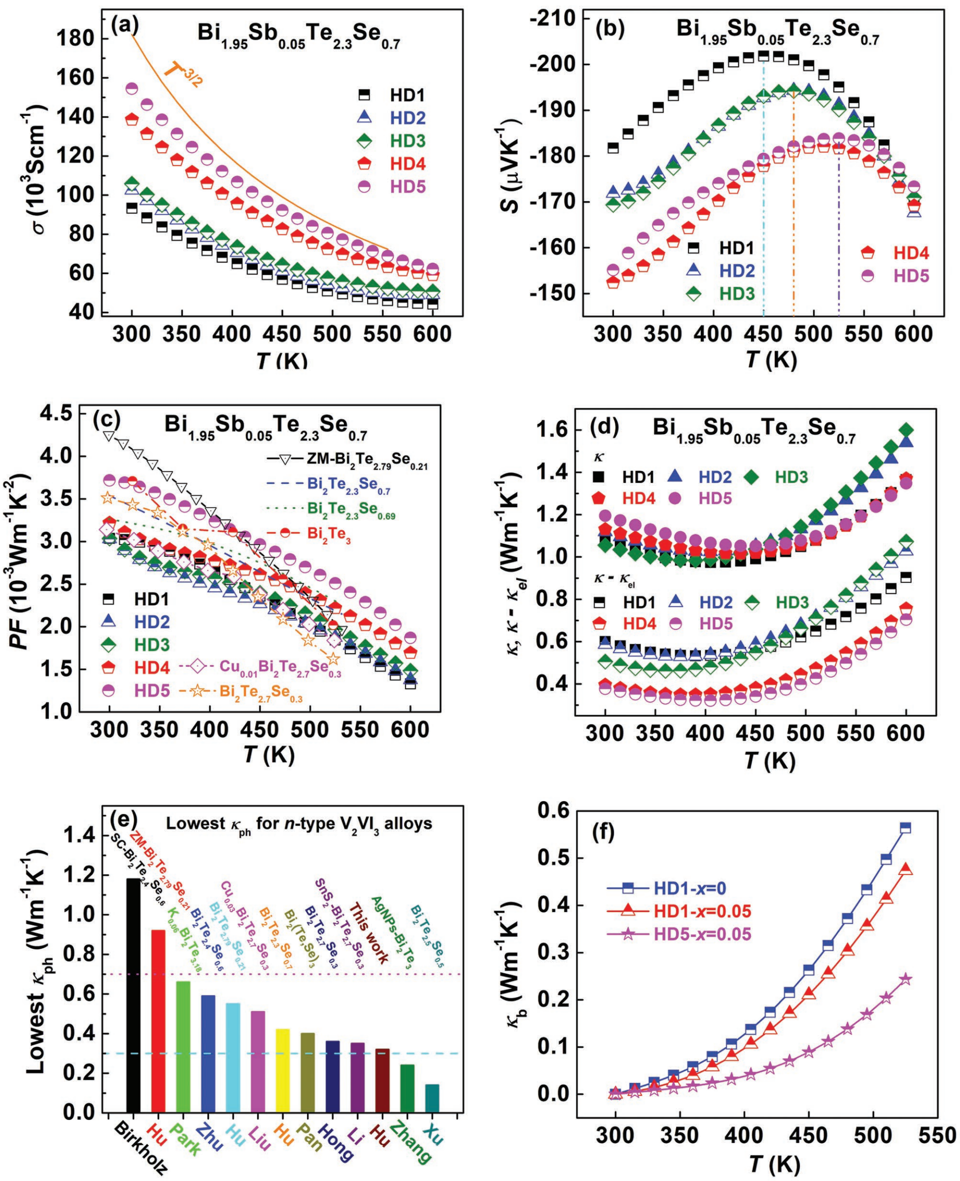

Figure 6. Temperature dependence of in-plane a) electrical conductivity, b) Seebeck coefficient, c) power factor, and d) total and lattice thermal conductivity for $Bi_{1.95}Sb_{0.05}Te_{2.3}Se_{0.7}$ with different HD count. e) Lowest lattice thermal conductivity in this work in comparison with those of other n-type V_2VI_3 materials.[8,10,22,36,37,44–46] f) Temperature dependence of bipolar thermal conductivity for $Bi_{2-x}Sb_xTe_{2.3}Se_{0.7}$ with different Sb content and HD count.

Progressive HD enhances the PF owing to the increased σ (Figure 6c). Specifically, the PF value at 300 K is 3.04×10^{-3} W m^{-1} K^{-1} for the HD1 sample, and it sharply increases to 3.72×10^{-3} W m^{-1} K^{-1} for the HD5 sample. The PF attained here was higher than those reported previously in n-type V_2VI_3 polycrystalline alloys,[8,10,45] and but lower than PF = 4.25×10^{-3} W m^{-1} K^{-1} for the ZM $Bi_2Te_{2.79}Se_{0.21}$,[8] which is ascribed to the stronger texture of the latter. It is also found that HD5 sample exhibit the highest PF above 450 K because the detrimental effect of minority carriers on the S is suppressed by promoting the donor-like effect without enlarging the E_g.

Figure 6d depicts the temperature dependence of κ and κ_{ph} for $Bi_{1.95}Sb_{0.05}Te_{2.3}Se_{0.7}$ samples with different HD count. As shown in Figure S11 of the Supporting Information, the heat capacity C_p values are practically unchanged with increasing hot deformation count, because HD itself does not change the chemical compositions (Table S1, Supporting Information). The κ shows small differences with the increase of hot deformation number. The κ_{el} is calculated by the Wiedemann–Franz law, $\kappa_{el} = L\sigma T$, where the Lorenz number L was roughly estimated using the formula $L = 1.5+\exp(-|S|/116)$.[47] (Figure S12, Supporting Information). Notably, progressive HD processing by itself can effectively diminish the κ_{ph} through complex microstructures. As mentioned above, the HD sample exhibits multiscale microstructures including atomic-scale point and line defects, nanoscale strain clusters, polycrystals, and distortions and micrometer-scale grain boundaries that can effectively scatter a wide spectrum of heat-carrying phonons. The κ_{ph} dramatically falls with increasing HD count. Typically, the room temperature κ_{ph} slightly drops from 0.6 W m^{-1} K^{-1} for the HD1 sample to 0.51 W m^{-1} K^{-1} for the HD3 sample, and then sharply decreases to 0.38 W m^{-1} K^{-1} for the HD5 one. It is concluded that larger deformation degree, more count and lower temperature leads to a lower κ_{ph}. In particular, the minimum κ_{ph} is only 0.31 W m^{-1} K^{-1} at 405 K for the HD5 sample, almost 40% reduction than that of HD1 counterpart. A careful comparison of κ_{ph} between this work and other results is plotted in Figure 6e. The observed κ_{ph} is one of the minimum values in V_2VI_3 alloys,[8,10,22,36,37,44–46] and close to those state-of-the-art TE materials with complex crystal structures and strong anharmonicity (Figure S13, Supporting Information).[48]

The flexion of κ–κ_{el} for all the samples was attributed to the thermally excited minority carriers, which is consistent with the change in S (Figure 6b). The bipolar effect is especially pronounced in narrow band gap V_2VI_3 materials, thereby limiting the zT values at high temperatures.[18,19] Again, suppressing the detrimental effect of intrinsic conduction is pivotal for high-temperature TE performance. The inflection point of κ–κ_{el} shifts to a higher temperature with increasing HD count, indicating that donor-like effect induced majority carrier concentration increment suppresses the bipolar effects.

In order to clarify the contribution of bipolar thermal conductivity κ_b at elevated temperatures, the κ_b as a function of temperature need to be identified. In cases where κ_b has no contribution, the relationship between the κ_{ph} and the reciprocal of temperature ($1/T$) is theoretically linear. Assuming a negligible effect of κ_b on κ before intrinsic excitation, the difference between the calculated κ_{ph} and experimental κ–κ_{el} is approximately equal to κ_b.[20] The κ_b of the representative samples (HD1-x = 0, HD1-x = 0.05, and HD5-x = 0.05) are presented in Figure 6f. With rising temperature, κ_b sharply increases because tremendous electron–hole pairs are thermally excited. The HD1-x = 0 sample shows a maximum κ_b of 0.56 W m^{-1} K^{-1} at 525 K, accounting for about 43% the total κ at corresponding temperature. After suitable doping Sb on Bi sites, slight reduction of κ_b is observed. Progressive HD further substantially depresses the κ_b. For HD5, the κ_b at 525 K is diminished to only 0.24 W m^{-1} K^{-1}, with a great decrease of 57% as compared with the x = 0 sample. As shown, promoting donor-like effect is an effective way to suppress κ_b instead of band gap enlargement.

Based on the analysis of texture evolution, intrinsic point defect, and multiscale microstructures, a question arises as to whether the synergistic compositional–mechanical–thermal effects created by progressive hot deformation combined with Sb-alloying lead to better TE properties? In progressively hot deformed x = 0.05 sample, the peak zT is further increased to 1.3 at 450 K for HD5 one, around 30% increment over the pristine $Bi_2Te_{2.3}Se_{0.7}$ counterpart (**Figure 7**a). This is a record zT value reported for the n-type V_2VI_3 materials (Figure 7b) with both the thermal and electrical properties measured along

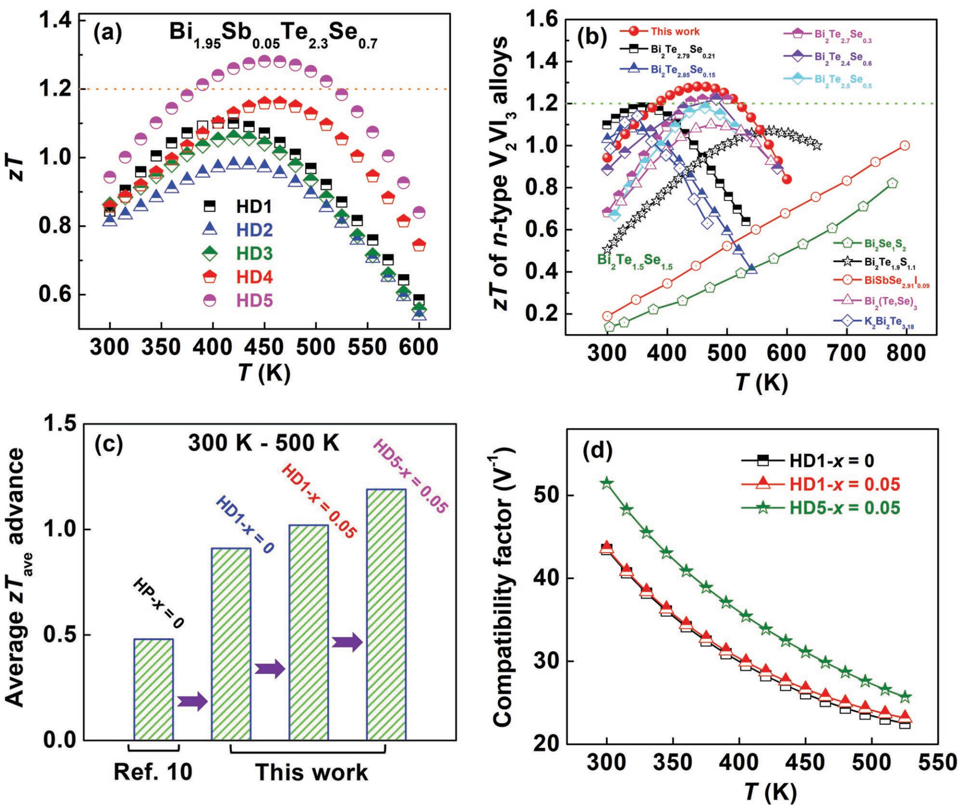

Figure 7. a) zT values as a function of temperature for $Bi_{1.95}Sb_{0.05}Te_{2.3}Se_{0.7}$ with different HD count. b) Temperature dependent zT for HD5 x = 0.05 sample, comparing with those of other high-zT n-type V_2VI_3 materials.[8,14,21,22,28,36,37],49,52,55 c) The main contributors to the average zT_{ave} advances between 300 and 500 K of the $Bi_{2-x}Sb_xTe_{2.3}Se_{0.7}$ alloys in this work. d) Compatibility factor as a function of temperature for $Bi_{2-x}Sb_xTe_{2.3}Se_{0.7}$ alloys.

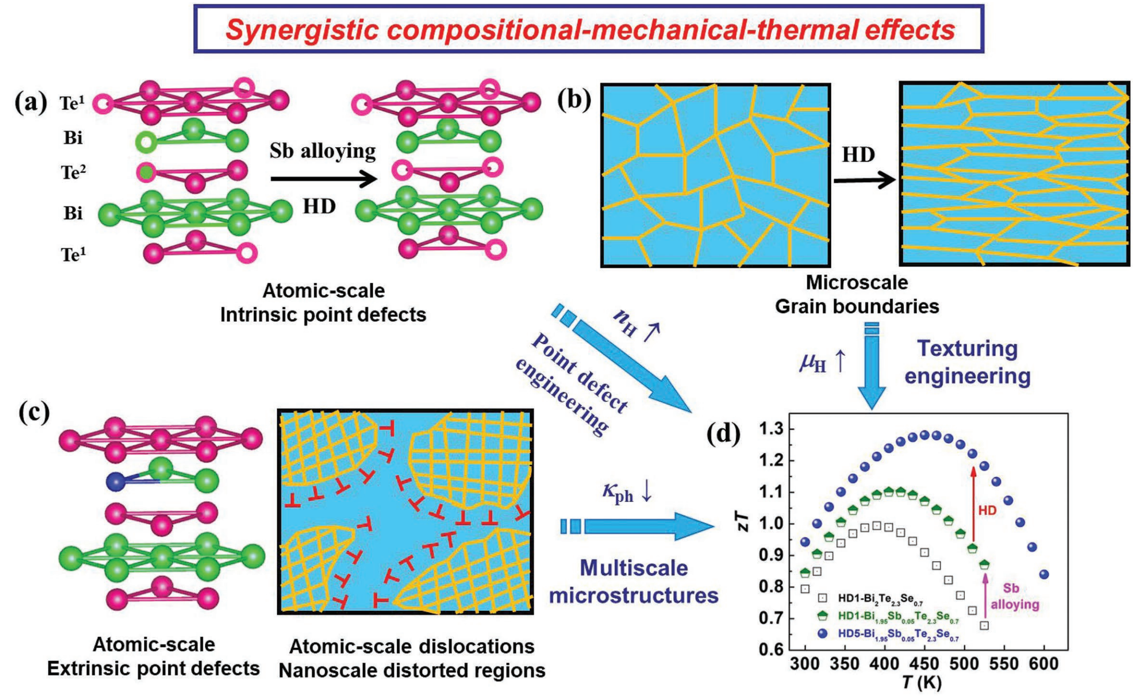

Figure 8. High zT for low-temperature power generation via synergistic compositional–mechanical–thermal effects through innovative hot deformation combined with Sb alloying. a) A schematic illustration showing the enhanced donor-like defects (i.e., anion vacancies) after suitable Sb alloying and progressive HD. Solid circles denote atoms, empty circles denote vacancies and red edge filled with green represents antisite defects. b) A schematic showing the enhanced texture after progressive HD. c) A schematic illustration showing the multiscale microstructures after Sb alloying and progressive HD. Red circles denote Te atoms, green circles denote Bi atoms, and blue circle denotes Sb atom. d) A comparison of the zT values of HD1-$Bi_2Te_{2.3}Se_{0.7}$, HD1-$Bi_2Sb_{0.05}Te_{2.3}Se_{0.7}$, and HD5-$Bi_2Sb_{0.05}Te_{2.3}Se_{0.7}$.

the in-plane direction.[8,14,21,22,28,36,37,45,46] Compared with other n-type materials with high zT, our sample is more competitive in the vicinity of 450 K, indicating promising application potential in low-temperature TE power generation. More importantly, the average zT_{ave} value is substantially improved via synergistic compositional–mechanical–thermal effects (Figure 7c). Typically, the average zT_{ave} value of HD5 is 1.2 in the range of 300–500 K. In addition, the compatibility factor is also enhanced during the progressive HD process (Figure 7d).

As illustrated in **Figure 8**, this work demonstrates the success of enhancing zT of n-type V_2VI_3 alloys, which match their p-type counterparts, by the synergy of point defect engineering, texture engineering, and multiscale microstructures. The efficacy of synergistic compositional–mechanical–thermal effects induced by innovative HD is thereby proved.

3. Conclusion

In this work, we implemented synergistic compositional–mechanical–thermal effects through progressive hot deformation toward a delicate balance between texture, extrinsic and intrinsic point defects, and multiscale microstructures in n-type quaternary V_2VI_3 alloys. These synergistic compositional–mechanical–thermal effects afforded a significantly extended parameter space for performance optimization. The details of texture evolution were systematically studied by X-ray powder diffraction, pole figures, and orientation distribution function. The integrated actions of larger magnitude, more counts and lower temperature of hot deformation gives rise to a stronger texture, which is comparable to that of zone melted ingots. The progressive hot deformation in conjunction with proper Sb alloying also facilitated the donor-like effect and increased the majority carrier concentration, successfully suppressing the detrimental effect of intrinsic conduction in absence of band gap enlargement. Meanwhile, owing to the multiscale microstructures that include atomic-scale point and line defects, nanoscale strain clusters, polycrystals, and distortions and microscale grain boundaries, an ultralow lattice thermal conductivity ≈0.31 W m^{-1} K^{-1} at 405 K was attained. As a result, a record zT of 1.3 at 450 K as well as high averaged zT_{ave} values of 1.2 between 300 and 500 K was achieved in five-time progressively hot deformed $Bi_{1.95}Sb_{0.05}Te_{2.3}Se_{0.7}$, which matches better with the p-type counterparts in device fabrication. The successful implementation of synergistic compositional–mechanical–thermal effects in bench mark n-type V_2VI_3 alloys marks a progress in both hot deformation technique and defect engineering.

4. Experimental Section

Sample Synthesis and Preparation: The n-type rhombohedral V_2VI_3 alloys were grown from the melt followed by hot deformation. Appropriate amounts of Bi (99.999%), Sb (99.999%), Te (99.999%), and Se (99.999%) were weighed according to the nominal compositions of $Bi_{2-x}Sb_xTe_{2.3}Se_{0.7}$ alloy (x = 0, 0.05, 0.10, 0.15, 0.20, and 0.25) and sealed into 10 mm-diameter quartz tubes evacuated at 10^{-3} Pa. These tubes were slowly heated to 1073 K in 5 h, dwelt for 10 h, and furnace-cooled to room temperature. The as formed ingots were crushed, ground into fine powders and then densified into Φ10 mm cylinders by spark plasma sintering at 723 K for 5 min with a 60 MPa uniaxial pressure. In a typical hot deformation process, the SPS samples were repressed in a much larger graphite die at 773 K for 5 min using the same stress. To promote the donor-like effect and the texture, progressive HD procedure is performed at a lower temperature (723 K), more counts (up to five times, the obtained samples were hereafter called HD1, HD2, HD3, HD4, and HD5, accordingly) and progressively larger deformation degree (up to 30 mm) at the same stress. More experimental details of HD can be found elsewhere.[4,8,10,20] Finally, highly densed (>95% of theoretical density) disk-shaped samples were obtained and subject to further microstructural and TE study.

Sample Characterization: X-ray diffraction data and pole figure measurement taken on the polished surfaces were obtained on a Bruker D8 Advance SS/18 kW diffractometer with the Cu 40 Kv 40 mA Kα radiation. The lattice parameters were refined by the Rietveld method using Topas 3.1 software. The chemical compositions were analyzed by JEOL JXA-8100 EDS. The samples for TEM JEOL ARM200F equipped with cold field emission gun, ASCOR probe corrector) were prepared by the conventional standard methods including cutting, grinding, dimpling, polishing and Ar-ion milling on a liquid nitrogen cooling stage.

A caveat in the determination of zT of textured V_2VI_3 materials is that all three TE properties must be measured in the same direction. In this work, all three TE properties of all the samples were measured along the in-plane direction (i.e., perpendicular to the HD pressing direction), if not otherwise noted. To this end, the in-plane thermal conductivity was measured using the method described in ref. [4]

The in-plane electrical conductivity σ and Seebeck coefficient S were simultaneously measured under helium atmosphere by using ZEM-2 (Ulvac-Riko, Japan). The thermal conductivity was calculated by using the equation $\kappa = \rho C_p D$, where ρ is the density of the bulk sample, C_p is the heat capacity and D is the thermal diffusivity, respectively. The ρ was estimated by using the sample dimensions and mass, and the C_P was measured on a Netzsch DSC 404C. The in-plane D was directly measured on a Netzsch LFA-457 instrument in the argon atmosphere. The Hall coefficients R_H were measured on a PPMS system (Quantum Design) with magnetic fields sweeping from −5T to 5T. The carrier concentrations n_H carrier mobility μ_H were calculated using the relation $n_H = 1/(eR_H)$ and $\mu_H = \sigma R_H$, respectively.

Supporting Information

Supporting Information is available from the Wiley Online Library or from the author.

Acknowledgements

The work is supported by the National Natural Science Foundation of China (51701126 and 51571144), the National Postdoctoral Program for Innovative Talents (BX201600110), the China Postdoctoral Science Foundation (2016M602515), and the Shenzhen Science and Technology Research Grant (JCYJ20150827155136104 and JCYJ20150324141711684). J.H. would like to acknowledge the financial support from NSFDMR1307740. S.J.P would like to acknowledge funding from the National University of Singapore.

Conflict of Interest

The authors declare no conflict of interest.

Keywords

microstructures, synergistic effects, textures, thermoelectrics, V_2VI_3

Received: May 25, 2018
Revised: June 14, 2018
Published online: July 13, 2018

[1] a) J. He, T. M. Tritt, *Science* **2017**, *357*, 1369; b) T. J. Zhu, Y. T. Liu, C. G. Fu, J. P. Heremans, J. G. Snyder, X. B. Zhao, *Adv. Mater.* **2017**, *29*, 1605884.
[2] J. P. Heremans, V. Jovovic, E. S. Toberer, A. Saramat, K. Kurosaki, A. Charoenphakdee, S. Yamanaka, G. J. Snyder, *Science* **2008**, *321*, 554.
[3] a) Y. Z. Pei, X. Shi, A. LaLonde, H. Wang, L. D. Chen, G. J. Snyder, *Nature* **2011**, *473*, 66; b) Y. Z. Pei, H. Wang, G. J. Snyder, *Adv. Mater.* **2012**, *24*, 6125; c) H. Wang, Y. Z. Pei, A. LaLonde, G. J. Snyder, *Adv. Funct. Mater.* **2013**, *23*, 1586.
[4] L. P. Hu, X. H. Liu, H. H. Xie, J. J. Shen, T. J. Zhu, X. B. Zhao, *Acta Mater.* **2012**, *60*, 4431.
[5] J. Sui, J. Li, J. He, Y. L. Pei, D. Berardan, H. Wu, N. Dragoe, W. Cai, L. D. Zhao, *Energy Environ. Sci.* **2013**, *6*, 2916.
[6] P. Puneet, R. Podila, S. Zhu, M. J. Skove, T. M. Tritt, J. He, A. M. Rao, *Adv. Mater.* **2013**, *25*, 1033.
[7] X. F. Meng, Z. H. Liu, B. Cui, D. D. Qin, H. Y. Geng, W. Cai, L. W. Fu, J. Q. He, Z. F. Ren, J. H. Sui, *Adv. Energy Mater.* **2017**, *7*, 1602582.
[8] a) L. P. Hu, H. J. Wu, T. J. Zhu, C. G. Fu, J. Q. He, P. J. Ying, X. B. Zhao, *Adv. Energy Mater.* **2015**, *5*, 1500411; b) L. P. Hu, H. L. Gao, X. H. Liu, H. H. Xie, J. J. Shen, T. J. Zhu, X. B. Zhao, *J. Mater. Chem.* **2012**, *22*, 16484.
[9] K. Biswas, J. He, I. D. Blum, C. I. Wu, T. P. Hogan, D. N. Seidman, V. P. Dravid, M. G. Kanatzidis, *Nature* **2012**, *489*, 414.
[10] L. P. Hu, T. J. Zhu, X. H. Liu, X. B. Zhao, *Adv. Funct. Mater.* **2014**, *24*, 5211.
[11] X. Shi, J. Yang, S. Q. Bai, J. H. Yang, H. Wang, M. F. Chi, J. R. Salvador, W. Q. Zhang, L. D. Chen, W. N. Winnie, *Adv. Funct. Mater.* **2010**, *20*, 755.
[12] a) T. J. Zhu, L. P. Hu, X. B. Zhao, J. He, *Adv. Sci.* **2016**, *3*, 1600004; b) Y. Liu, M. Zhou, J. He, *Scr. Mater.* **2016**, *111*, 39.
[13] W. M. Yim, F. D. Rosi, *Solid-State Electron.* **1972**, *15*, 1121.
[14] a) S. Y. Wang, G. J. Tan, W. J. Xie, G. Zheng, H. Li, J. H. Yang, X. F. Tang, *J. Mater. Chem.* **2012**, *22*, 20943; b) S. Y. Wang, Y. Sun, J. Yang, B. Duan, L. Wu, W. Zhang, J. H. Yang, *Energy Environ. Sci.* **2016**, *9*, 3436.
[15] B. Poudel, Q. Hao, Y. Ma, Y. Lan, A. Minnich, B. Yu, X. Yan, D. Wang, A. Muto, D. Vashaee, X. Chen, J. Liu, M. S. Dresselhaus, G. Chen, Z. Ren, *Science* **2008**, *320*, 634.
[16] J. Li, Q. Tan, J. F. Li, D. W. Liu, F. Li, Z. Y. Li, M. Zou, K. Wang, *Adv. Funct. Mater.* **2013**, *23*, 4317.
[17] S. Kim, K. H. Lee, H. A. Mun, H. S. Kim, S. W. Hwang, J. W. Roh, D. J. Yang, W. H. Shin, X. S. Li, Y. H. Lee, G. J. Snyder, S. W. Kim, *Science* **2015**, *348*, 109.
[18] Z. J. Xu, H. J. Wu, T. J. Zhu, C. G. Fu, X. H. Liu, L. P. Hu, J. He, J. Q. He, X. B. Zhao, *NPG Asia Mater.* **2016**, *8*, e302.
[19] L. P. Hu, T. J. Zhu, X. Q. Yue, X. H. Liu, Y. G. Wang, Z. J. Xu, X. B. Zhao, *Acta Mater.* **2015**, *85*, 270.
[20] L. P. Hu, T. J. Zhu, Y. G. Wang, H. H. Xie, Z. J. Xu, X. B. Zhao, *NPG Asia Mater* **2014**, *6*, e88.
[21] W. S. Liu, K. C. Lukas, K. McEnaney, S. Lee, Q. Zhang, C. P. Opeil, G. Chen, Z. F. Ren, *Energy Environ. Sci.* **2013**, *6*, 552.
[22] M. Hong, T. C. Chasapis, Z. G. Chen, L. Yang, M. G. Kanatzidis, G. J. Snyder, J. Zou, *ACS Nano* **2016**, *10*, 4719.

[23] Y. Xiao, J. Y. Yang, Q. H. Jiang, L. W. Fu, Y. B. Luo, M. Liu, D. Zhang, M. Y. Zhang, W. X. Li, J. Y. Peng, F. Q. Chen, *J. Mater. Chem. A* **2014**, *2*, 20288.
[24] Y. Zheng, Q. Zhang, X. Su, H. Xie, S. Shu, T. Chen, G. Tan, Y. Yan, X. Tang, C. Uher, G. J. Snyder, *Adv. Energy Mater.* **2015**, *5*, 1401391.
[25] H. J. Goldsmid, *J. Appl. Phys.* **1961**, *32*, 2198.
[26] J. M. Schultz, W. A. Tiller, J. P. McHugh, *J. Appl. Phys.* **1962**, *33*, 2443.
[27] L. D. Zhao, B. P. Zhang, J. F. Li, H. L. Zhang, W. S. Liu, *Solid State Sci.* **2008**, *10*, 651.
[28] Z. L. Tang, L. P. Hu, T. J. Zhu, X. H. Liu, X. B. Zhao, *J. Mater. Chem. C* **2015**, *3*, 10597.
[29] F. Hao, P. Qiu, Y. Tang, S. Bai, T. Xing, H. S. Chu, Q. Zhang, P. Lu, T. Zhang, D. Ren, J. Chen, X. Shi, L. Chen, *Energy Environ. Sci.* **2016**, *9*, 3120.
[30] L. P. Hu, Y. M. Guo, J. Q. Li, W. Q. Ao, F. S. Liu, C. H. Zhang, Y. Li, X. R. Zeng, *Mater. Res. Bull.* **2018**, *99*, 377.
[31] I. Teramoto, S. Takayanagi, *J. Phys. Chem. Solids* **1961**, *19*, 124.
[32] H. Cho, J. H. Kim, S. Y. Back, K. Ahn, J. S. Rhyee, S. D. Park, *J. Alloys Compd.* **2018**, *731*, 531.
[33] Y. Wu, R. Zhai, T. Zhu, X. Zhao, *Mater. Today Phys.* **2017**, *2*, 62.
[34] K. Yamauchi, M. Takashiri, *J. Alloys Compd.* **2017**, *698*, 977.
[35] J. Jiang, L. D. Chen, S. Q. Bai, Q. Yao, Q. Wang, *Mater. Sci. Eng. B* **2005**, *117*, 334.
[36] B. Zhu, Z. Y. Huang, X. Y. Wang, Y. Yu, L. Yang, N. Gao, Z. G. Chen, F. Q. Zu, *Nano Energy* **2017**, *42*, 8.
[37] Y. Pan, J. F. Li, *NPG Asia Mater.* **2016**, *8*, e275.
[38] X. A. Fan, J. Y. Yang, W. Zhu, S. Q. Bao, X. K. Duan, C. J. Xiao, K. Li, *J. Phys. D: Appl. Phys.* **2007**, *40*, 5727.
[39] S. J. Hong, B. S. Chun, *Mater. Res. Bull.* **2003**, *38*, 599.
[40] S. D. Bhame, D. Pravarthana, W. Prellier, J. G. Noudem, *Appl. Phys. Lett.* **2013**, *102*, 211901.
[41] A. K. Bohra, R. Bhatt, A. Singh, R. Basu, S. Bhattacharya, K. N. Meshram, S. Ahmad, A. K. Debnath, A. K. Chauhan, P. Bhatt, K. Shah, K. Bhotkar, S. Sharma, D. K. Aswal, K. P. Muthe, S. C. Gadkari, *Energy Convers. Manage.* **2017**, *145*, 415.
[42] C. Zhang, X. A. Fan, J. Hu, C. Jiang, Q. Xiang, G. Li, Y. Li, Z. He, *Adv. Eng. Mater.* **2017**, *19*, 1600696.
[43] F. K. Lotgering, *J. Inorg. Nucl. Chem.* **1959**, *9*, 113.
[44] U. Birkholz, *Z. Naturforsch. A* **1958**, *13*, 780.
[45] a) R. S. Zhai, L. P. Hu, H. J. Wu, Z. J. Xu, T. J. Zhu, X. B. Zhao, *ACS Appl. Mater. Interfaces* **2017**, *9*, 28577; b) W. S. Liu, Q. Zhang, Y. Lan, S. Chen, X. Yan, Q. Zhang, H. Wang, D. Wang, G. Chen, Z. Ren, *Adv. Energy Mater.* **2011**, *1*, 577; c) X. Yan, B. Poudel, Y. Ma, W. S. Liu, G. Joshi, H. Wang, Y. Lan, D. Wang, G. Chen, Z. F. Ren, *Nano Lett.* **2010**, *10*, 3373.
[46] a) K. Park, K. Ahn, J. Cha, S. Lee, S. I. Chae, S. P. Cho, S. Ryee, J. Im, J. Lee, S. D. Park, M. J. Han, I. Chung, T. Hyeon, *J. Am. Chem. Soc.* **2016**, *138*, 14458; b) B. Xu, T. Feng, M. T. Agne, L. Zhou, X. Ruan, G. J. Snyder, Y. Wu, *Angew. Chem., Int. Ed.* **2017**, *56*, 3546; c) S. Li, X. Liu, Y. Liu, F. Liu, J. Luo, F. Pan, *Nano Energy* **2017**, *39*, 297; d) Q. Zhang, X. Ai, L. Wang, Y. Chang, W. Luo, W. Jiang, L. Chen, *Adv. Funct. Mater.* **2015**, *25*, 966.
[47] H. S. Kim, Z. M. Gibbs, Y. Tang, H. Wang, G. J. Snyder, *APL Mater.* **2015**, *3*, 041506.
[48] a) G. J. Snyder, M. Christensen, E. Nishibori, T. Caillat, B. B. Iversen, *Nat. Mater.* **2004**, *3*, 458; b) L. D. Zhao, S. H. Lo, Y. Zhang, H. Sun, G. Tan, C. Uher, C. Wolverton, V. P. Dravid, M. G. Kanatzidis, *Nature* **2014**, *508*, 373.